International Journal on Recent and Innovation Trends in Computing and Communication
ISSN: 2321-8169 Volume: 11 Issue: 8s
DOI: https://doi.org/10.17762/ijritcc.v11i8s.7205
***Article Received**: 23 April 2023 **Revised:** 10 June 2023 **Accepted:** 28 June 2023*

Deep Convolutional Attention based Bidirectional Recurrent Neural Network for Measuring Correlated Colour Temperature from RGB Images

[1]Sanket Satish Mane, [*2]Ajit Kumar Santra
[1]Research Scholar, School of Electronics Engineering,
VIT University, Vellore, Tamil Nadu, India.
Email: sanketsatish.mane2016@vitstudent.ac.in
[2]Senior Professor, School of Information Technology,
VIT University, Vellore, Tamil Nadu, India.
*Email: ajitkumar@vit.ac.in
[* indicates Corresponding Author]

Abstract: Information on the connected colour temperature, which affects the image due to the surrounding illumination, is critical, particularly for natural lighting and capturing images. Several methods are introduced to detect colour temperature precisely; however, the majority of them are difficult to use or may generate internal noise. To address these issues, this research developed a hybrid deep model that properly measures temperature from RGB images while reducing noise. The proposed study includes image collection, pre-processing, feature extraction and CCT evaluation. The input RGB pictures are initially generated in the CIE 1931 colour space. After that, the raw input samples are pre-processed to improve picture quality by performing image cropping and scaling, denoising by hybrid median-wiener filtering and contrast enhancement via Rectified Gamma-based Quadrant Dynamic Clipped Histogram Equalisation (RG_QuaDy_CHE). The colour and texture features are eliminated during pre-processing to obtain the relevant CCT-based information. The Local Intensity Grouping Order Pattern (LIGOP) operator extracts the texture properties. In contrast, the colour properties are extracted using the RGB colour space's mean, standard deviation, skewness, energy, smoothness and variance. Finally, using the collected features, the CCT values from the submitted images are estimated using a unique Deep Convolutional Attention-based Bidirectional Recurrent Neural Network (DCA_BRNNet) model. The Coati Optimisation Algorithm (COA) is used to improve the performance of a recommended classifier by modifying its parameters. In the Result section, the suggested model is compared to various current techniques, obtaining an MAE value of 529K and an RMSE value of 587K, respectively.

Keywords: colour space, spectrum, monochromatic lights, image clarity and pixel value, gamma correlation, histogram clipping, spatial variance

I. INTRODUCTION

Digital image processing has recently attracted attention as a solution to circumvent this constraint [1]. The technique of analyzing a digital image to extract required information is known as digital image processing. A digital picture comprises RGB (red, green and blue) standards ranging from 0 to 255 allocated to each pixel (in the case of a white and black image, the pixels are assigned grey values ranging from 0 to 255). The colour of the influencing light is displayed in a scene's correlating colour temperature (CCT), which is measured in Kelvin (K)) [2]. The CCT value can be used to determine how an object will appear in an image. Circadian lighting is becoming more popular in industries such as healthcare, industry and business, requiring indoor artificial light colour tuning [3]. This is achieved by adapting the CCT and brightness of the artificial illumination to the lighting conditions outside. Determining the light source CCT in photography is essential for determining the shot's colour output [4]. White balance, a camera setting that may be changed by the photographer, is connected to the CCT of light that controls the scene. CCT data regarding the light source at a certain location is therefore essential in a human-centered lighting and photography technology [5].

The hue-heat idea is widely cited to explain how CCT could affect thermal perception. According to this concept, blue colours provide a colder temperature impression, whereas red/yellow colours produce a warmer sense of the environmental atmosphere [6]. White light that has a high CCT is perceived as being bluer than white light that has a low CCT, which could be perceived as being more yellowish. Therefore, it is anticipated that exposure to high CCT will promote thermal comfort in thermally warm situations as opposed to low CCT and vice versa [7]. Luminous and non-luminous colour may have quite different impacts, but researchers have explored this cross-modal colour-temperature relationship using colored surfaces, goggles, virtual reality and lighting [8]. Inter-

International Journal on Recent and Innovation Trends in Computing and Communication
ISSN: 2321-8169 Volume: 11 Issue: 8s
DOI: https://doi.org/10.17762/ijritcc.v11i8s.7205
***Article Received**: 23 April 2023 **Revised:** 10 June 2023 **Accepted:** 28 June 2023*

individual differences exist in the colour-temperature relationship as colour-temperature associations change during growth and adulthood [9]. In addition, recent research found a link between thermal comfort in laboratory and visual comfort (the total comfort perception of light) and outdoor settings.

Due to the wide inter- and intra-individual variation in which lighting settings are deemed visually pleasing, using a light setting to improve thermal comfort and visual comfort is complicated [10]. Personal variables such as gender, general preferences or age may influence inter-individual variance to some extent. Intra-individual variation may be influenced by factors such as a person's mental state (e.g., level of attentiveness) or the task at hand [11, 12]. Providing individuals with control over the light setting is one method to address this unpredictability. Individual preferences can be provided for by adjusting the objective light settings. Furthermore, it provides a sense of control linked to decreased stress reactivity [13, 14]. In addition, controlling one unpleasant stimulus may attenuate the adverse effects of a different unpleasant stimulus [15], implying that controlling illumination may further alleviate heat discomfort.

A Motivation

Digital image processing has recently gained interest as a remedy to this restriction. Digital image processing is the process of examining digital images to extract information. The appearance of a recognized element in an image may be determined using the CCT value. Circadian lighting is increasingly common in healthcare, industry, and business, demanding indoor artificial light colour calibration. However, effective CCT measurement techniques are rare, and most function poorly. As a result, this study inspired the researchers to perform a study and construct an effective CCT measurement technique based on deep learning models. The following are the key contributions:

- To produce the input RGB images, the CIE 1931 colour space is used, and the input samples are pre-processed to increase the quality of the images by cropping and resizing the images, denoising using a hybrid median-wiener filter and enhancing contrast using a technique called Rectified Gamma based Quadrant Dynamic Clipped Histogram Equalisation (RG_QuaDy_CHE).
- The Local Intensity Grouping Order Pattern (LIGOP) operator extracts the texture features. In contrast, the RGB colour space's mean, standard deviation, skewness, energy, smoothness and variance are used to extract colour features.
- To estimate the CCT values, a novel Deep Convolutional Attention-based Bidirectional Recurrent Neural Network (DCA_BRNNet) model is introduced.
- To fine-tune the parameters of a suggested classifier, the Coati Optimisation Algorithm (COA) is used and produces better performance results.
- In the result section, MSE and RMSE compare existing methods and achieve the best values.

The rest of the sections are organized: Section 2 represents the related work, Section 3 represents the proposed methodology, Section 4 represents the result and discussion, and Section 5 represents the conclusion and future scope.

II. RELATED WORKS

By using the camera as the only sensor and basing their method on the lighting conditions of the surrounding area, Kamath et al.'s [16] method predicts the corresponding color temperature in an image. A DSLR camera was used to take the image, which was then attached to a Macbeth ColorChecker chart. Using the CIEDE2000 technique, color differences are determined from the pixel data of the six spectrally neutral patches on a ColorChecker chart. Six neutral patches' hue values are used as inputs for the Bayesian neural network-based method, which predicts the CCT value. However, this approach provides excellent precision only when the focal length was fixed.

In order to measure the short-wavelength-ratio-based color temperature of natural light, Oh et al. [17] present a real-time method. To identify the factors necessary to accurately determine the colour temperature of natural light, a study of the relationships between the characteristics of natural light collected with a spectroradiometer was first conducted. In order to calculate the short-wavelength ratio of natural light, chromaticity coordinates (x and y), which are RGB sensor output values, were used. The short-wavelength ratio was then used to construct an equation that estimated the colour temperature of natural light. The created equation was also used to establish the color temperature of real-time natural light, which serves as a representation of the wavelength characteristics, after creating an RGB-sensor-based device. However, this approach had an error rate of 0.903%.

Based on the prediction models, Oh et al. [18] created the warm-cool-based CCT idea. It was calculated an on-Planckian with the same number of warm-cold feelings as the off-Planckian test point. It follows the same basic logic as the current CCT, which assigns a single number, but it was based on warm-cool emotions instead. The colour fidelity was its major drawback.

Magnusson et al. [19] provide a standardized approach for producing realistic colour pictures of HSI. The method converts every observable spectral band to the XYZ colour system, using D65 as the reference illuminant and then converts the XYZ to

International Journal on Recent and Innovation Trends in Computing and Communication
ISSN: 2321-8169 Volume: 11 Issue: 8s
DOI: https://doi.org/10.17762/ijritcc.v11i8s.7205
***Article Received**: 23 April 2023 **Revised:** 10 June 2023 **Accepted:** 28 June 2023*

the sRGB (standard Red, Green, Blue) colour space. To boost contrast, the image was gamma-corrected and then thresholded. However, despite the saturation, the approach was complicated and inefficient.

Kompier et al. [20] found that sudden illuminance and/or CCT changes resulted in distinct temporal response dynamics for subjectively assessed appraisal, mood, and alertness. Illuminance and CCT didn't structurally combine with these markers, but each affected a selection. Responses to sudden changes in illuminance and CCT were always instantaneous and exclusive between the subjective markers. The illumination changes did not affect thermal comfort or thermoregulation. However, the substantial influence discovered may be due to the different melanopic activation caused by the opposing light conditions.

Problem statement

To represent the colour of light sources, CCT must be evaluated. The correct measurement of CCT in photometric research is difficult due to several difficulties. According to current research, the range of CCT in the environment significantly influences human behaviour and perception. As a result, such influences have a far greater impact on daily life. To reduce these problems, the proposed research used an efficient deep learning system to calculate CCT values from the input images.

III. PROPOSED METHODOLOGY

To accurately depict the colour of light sources, CCT evaluation is crucial. The proposed research performs a variety of crucial steps, including image capture, pre-processing, feature extraction and CCT measurement to perform CCT estimation. The CIE 1931 colour space is initially used to produce the input RGB images. After that, the raw input samples are pre-processed to increase the quality of the images by cropping and resizing the images, denoising using a hybrid median-wiener filter and enhancing contrast using a technique called Rectified Gamma based Quadrant Dynamic Clipped Histogram Equalisation (RG_QuaDy_CHE). To acquire the necessary CCT-based information, colour and texture characteristics are extracted after pre-processing. The Local Intensity Grouping Order Pattern (LIGOP) operator extracts texture characteristics. In contrast, the RGB colour space's Mean, Standard Deviation, Skewness, Energy, Smoothness And Variance extract colour features. Finally, a novel Deep Convolutional Attention-based Bidirectional Recurrent Neural Network (DCA_BRNNet) model is introduced that uses the recovered features to evaluate the CCT values from the provided images. The Coati Optimisation Algorithm (COA) is used to fine-tune the parameters of a suggested classifier and produces better performance results. Figure 1 represents the basic block diagram of a proposed model.

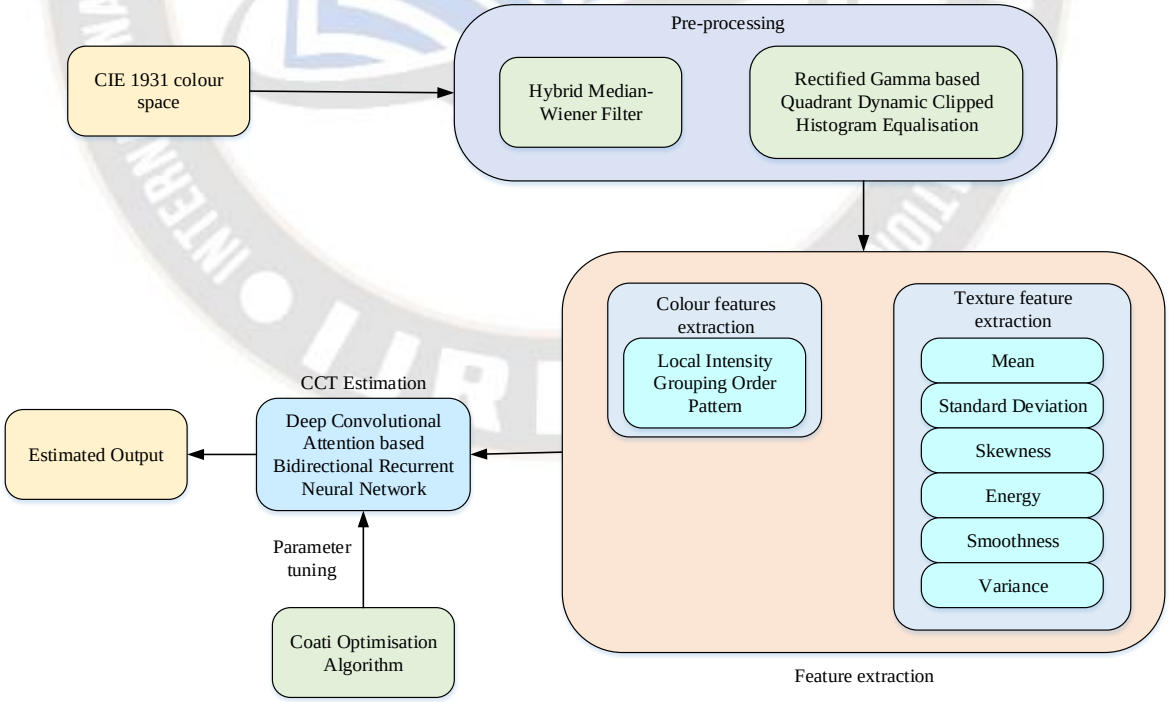

Figure 1: Basic block diagram of the proposed model

International Journal on Recent and Innovation Trends in Computing and Communication
ISSN: 2321-8169 Volume: 11 Issue: 8s
DOI: https://doi.org/10.17762/ijritcc.v11i8s.7205
***Article Received**: 23 April 2023 **Revised:** 10 June 2023 **Accepted:** 28 June 2023*

A. Pre-processing

The CIE 1931 colour spaces are the initial quantitative connections among the distributions of electromagnetic visible spectrum wavelengths and physiologically experienced colours in human colour vision. A complete knowledge of the mathematical relationships defining these colour spaces is essential when employing, illuminated displays recording devices and colour inks like digital cameras. Humans can only detect radiation with wavelengths between 380 and 780 nm, which is the definition of light. Visible light is a popular name for this radiation. As a result, the visible band may be used to refer to the space between the ultraviolet and infrared bands. The data available on this band is connected to how people generally observe images. The CIE 1931 colour space is used to create the input RGB pictures for this study. $\hat{g}(\pi), \hat{b}(\pi) and\ \hat{r}(\pi)$ are the three functions that make up the CIE RGB colour matching functions (CMF).

These colour-matching methods are employed to convert the visible band light signal (380–780 nm) into the tristimulus values X, Y and Z. According to CMF, any monochromatic light U_{π_i} with π_i wavelength has the same summing composition of R, G and B colours and additives. A light signal P can be described as the totality of monochromatic lights, where each light is specified as light U_{π_i} scaled by a factor of P_i. Tristimulus values may be computed using CIE RGB colour-matching functions as indicated in Equation (1) for illumination with a spectral distribution.

$$\begin{aligned} G &= \int_{380}^{780} \hat{g}(\pi) P(\pi) d\pi \\ R &= \int_{380}^{780} \hat{r}(\pi) P(\pi) d\pi \\ B &= \int_{380}^{780} \hat{b}(\pi) P(\pi) d\pi \end{aligned} \tag{1}$$

The CIE 1931 RGB and the CIE 1931 XYZ colour spaces are transformed linearly. This indicates an invertible transition between the visible light spectrum and the colour space produced by human sight. A transformation matrix, which is indicated by the symbol N is used to execute the conversion among RGB and XYZ.

Numerous N conversion matrices by the RGB Workspace region and reference white are documented. The most commonly utilized N matrix in research is CIE XYZ to sRGB, which uses CIE Standard Illuminant D65 as the baseline white. This investigation employed the values of identical conversion matrix and D65 standard white. In Equations (2) and (3), the corresponding numerical values concerning N and N^{-1} are provided.

$$\begin{bmatrix} X \\ Y \\ Z \end{bmatrix} = \overbrace{\begin{bmatrix} 0.412 & 0.357 & 0.180 \\ 0.212 & 0.715 & 0.072 \\ 0.019 & 0.119 & 0.950 \end{bmatrix}}^{N} \begin{bmatrix} R \\ G \\ B \end{bmatrix} \tag{2}$$

$$\begin{bmatrix} R \\ G \\ B \end{bmatrix} = \overbrace{\begin{bmatrix} 3.240 & -1.537 & -0.498 \\ -0.968 & 1.875 & 0.041 \\ 0.055 & -0.204 & 1.057 \end{bmatrix}} \begin{bmatrix} X \\ Y \\ Z \end{bmatrix} \tag{3}$$

As the result of a transition between the X, Y and Z values, the Y value denotes the signal's strength. Considering that the mid-band cone cells associated with the colour green are the primary ones used by the human eye to process light. In order to determine chromaticity, equation (4) employs the X, Y and Z parameters obtained from the RGB to XYZ conversion. The balance between a light stream's main wavelengths is defined by the term "XYZ to xy conversion," which describes this conversion.

$$x = \frac{X}{X + Y + Z} \tag{4}$$

$$y = \frac{Y}{X + Y + Z} \tag{5}$$

$$z = \frac{Z}{X + Y + Z} \tag{6}$$

An illustration of coordinate data in two dimensions is a CIE xy chromaticity diagram. By computation $z = 1 - x - y$, which means that $x + y + z = 1$. The values of y and x relate to this representation. In CIE 1931 colour space, the y and x coordinate are shown with a point. A colour gamut diagram is another name for this illustration. The whole range of colours that are discernible to the human eye is known as the colour gamut.

This procedure converts the RGB values of pixels generated from RGB pictures into CIE 1931 xy coordinate. With the aid of the N matrix, the RGB signal is transformed into XYZ in the initial stage. The XYZ standards are then transformed into xy standards in the second stage using the formulae provided in Equations (4), (5) and (6). Visible light has several uses, including lighting, astrophysics, astronomy, printing, manufacturing, photography, videography and building. It has a significant influence on how people behave and perceive their surroundings.

1) Hybrid Median-Wiener Filtering

Generally, noise-prone declined images are repaired using an appropriate method, like filtering. This may be mentioned mathematically as follows:

International Journal on Recent and Innovation Trends in Computing and Communication
ISSN: 2321-8169 Volume: 11 Issue: 8s
DOI: https://doi.org/10.17762/ijritcc.v11i8s.7205
***Article Received**: 23 April 2023 **Revised:** 10 June 2023 **Accepted:** 28 June 2023*

$$G(u,v) = a(u,v) * d(u,v) + N(u,v) \quad (7)$$

$$F(u,v) = Q[G(u,v)] \quad (8)$$

where $a(u,v)$ is the obtained image, $d(u,v)$ is the reduction function," "symbolizes convolution, $N(u,v)$ denotes noise including Gaussian noise, $G(u,v)$ represents the output degraded image and $F(u,v)$ is the final result image after applying the procedure Q. The deteriorated images were put into a typical noise cancellation filter to get denoised RGB images. Non-linear spatial domain noise reduction filters like the median and Wiener are frequently used to produce denoised images. The following steps should be followed to improve the image quality: The spatial noise elimination filter is set up first using a mask matrix of dimension $x \times y$. Following that, with the degraded image matching with the mask pixel dimensions, the mask matrix is utilized to compute the updated pixel value compared to the mask pixel value. The median filter converts each pixel value into a median value corresponding to the mask matrix at its centre pixel value. This strategy is useful for removing abnormalities without losing the image's clarity. The Wiener filter is illustrated as follows:

$$\lambda = \frac{1}{XY} \sum_{x,y \in \mu} r(x,y) \quad (9)$$

$$\eta^2 = \frac{1}{XY} \sum_{x,y \in \mu} r(x,y) - \lambda^2$$

where $x \times y$ is the dimension of a neighbourhood area μ within the mask, $r(x,y)$ denotes each pixel in the space μ, η^2 indicates the variance of the Gaussian noise in an image and λ denotes the mean. The predicted values denote the new pixels as $W_f(x,y)$, and the Wiener filter is then applied to those pixels.

$$W_f(x,y) = \lambda + \frac{\eta^2 - V^2}{\eta^2} \cdot (r(x,y) - \lambda) \quad (10)$$

Where V^2 is the noise variance parameter of the Wiener filter that will be applied by the mask matrix. The image was cropped and resized to a final size of 400 × 600 pixels. It is designed to make computations during the feature extraction process easier. This model improves the image quality by performing image cropping, resizing and denoising, while the contrast is enhanced by Rectified Gamma based Quadrant Dynamic, Clipped Histogram Equalization (RG_QuaDy_CHE).

2) Contrast enhancing using RG_QuaDy_CHE

The formula $z(x,y) = \{g(x,y), b(x,y), r(x,y)\}$ describes a colour image. Pixel coordinates are indicated by (x,y), where $y = 1 \ldots Y, x = 1, \ldots X$ and the height and width of an image are represented by Y and X.

The colour vibrancy of an image is enhanced by stretching each colour channel. First stretched is the red colour, which is identified by,

$$r(x,y) \leftarrow \frac{r(x,y) - \min\{r(x,y)\}}{\max\{r(x,y)\} - \min\{r(x,y)\}} \quad (11)$$

Min and max represent the values achieved over all pixels at the minimal and maximum levels. The colour channels for green $g(x,y)$ and blue $b(x,y)$ are also distorted. Following this procedure, the HSI colour space is created from each colour channel. The intensity (i) channel in this colour space is further treated to improve contrast. The RGB-HSI colour conversion is described as

$$[h(x,y), s(x,y), i(x,y)] = E_{rgb}^{hsi}[r(x,y), g(x,y), b(x,y)] \quad (12)$$

Where E_{rgb}^{hsi} is the symbol for the RGB-to-HSI conversion. By keeping the saturation (s) and hue (h) channel to an ideal, the intensity (i)channel must be processed or improved separately to provide improved image quality. The intensity is described by:

$$i(x,y) \leftarrow \frac{\{r(x,y) + g(x,y) + b(x,y)\}}{3} \quad (13)$$

The rectified gamma correlation effectively determines the intensity channel conversion function depending on the properties of an input colour image. This algorithm maintains the mean brightness without any unwanted artefacts and improves contrast. The proposed model computes the intensity channel conversion as follows:

$$C(x,y) = E\{i(x,y)\} = i(x,y) \left(\frac{\{i(x,y)\}}{i_{\max}} \right)^{\hat{\gamma}} \quad (14)$$

Here, the cumulative distribution function (CDF) is used to determine $i_{\max}$, the highest intensity levels in an image and $\hat{\gamma}$ is the gamma value.

$$\hat{\gamma}(j) = 1 - CDF(j) \quad (15)$$

Where $CDF(j)$ denotes a CDF.

International Journal on Recent and Innovation Trends in Computing and Communication
ISSN: 2321-8169 Volume: 11 Issue: 8s
DOI: https://doi.org/10.17762/ijritcc.v11i8s.7205
***Article Received**: 23 April 2023 **Revised:** 10 June 2023 **Accepted:** 28 June 2023*

The appropriate selection of maxima and minima is not aided by applying HE before partitioning. An unnatural-looking output image is the result of this inaccurate identification. The input histogram is divided into four pieces using the mean value according to the proposed RG_QuaDy_CHE model. Without any noise or saturation of the intensity, the proposed method generates optimal output images. The input image's mean values for intensity are determined using the formula:

$$I_{mean} = \frac{1}{P}\sum_{j=I_0}^{I_4} H(j)\times j \tag{16}$$

$$I_{mean1} = \frac{1}{P}\sum_{j=I_{mean}}^{I_4} H(j)\times j \tag{17}$$

When lower and higher intensity values are identified by I_0 *and* I_4, the number of pixels is identified by P and $H(j)$ is the histogram's representation. Equations (18) and (19) determine the three intervals and calculate the associated PDF and CDF for the mean.

$$\begin{Bmatrix} PDF_1(j) = \dfrac{H(j)}{P_1} \ for\ I_0 \le j < I_{mean} - 1 \\ PDF_2(j) = \dfrac{H(j)}{P_2} \ for\ I_{mean} \le j < I_{mean1} - 1 \\ PDF_3(j) = \dfrac{H(j)}{P_3} \ for\ I_{mean1} \le j \le I_4 \end{Bmatrix} \tag{18}$$

$$\begin{Bmatrix} CDF_1(j) = \sum_{j=I_0}^{I_{mean}} PDF_1(j) \\ CDF_2(j) = \sum_{j=I_{mean}}^{I_{mean1}} PDF_2(j) \\ CDF_3(j) = \sum_{j=I_{mean1}}^{I_4} PDF_3(j) \end{Bmatrix} \tag{19}$$

P_1, P_2 *and* P_3 represent how many pixels are connected to the specific intensity level. It is discovered that the separation points I_1, I_2 *and* I_3 are:

$$I_1 = j, where CDF_1(j) \cong 0.33 \tag{20}$$

$$I_2 = j, where CDF_2(j) \cong 0.66 \tag{21}$$

$$I_3 = j, where CDF_3(j) \cong 0.83 \tag{22}$$

The initial histogram's intensity which is from $[I_0 : I_4]$ is divided into four pieces. The input histogram K is divided into four sub-histograms K_1, K_2, K_3 *and* K_4 with the ranges $[I_0 : I_1], [I_{1+1} : I_2], [I_{2+1} : I_3]$ *and* $[I_{3+1} : I_4]$, in this instance.

To prevent over-enhancement and the intensity-saturated effect, histogram clipping regulates the rate of improvement. The threshold level for each sub-histogram in this method is based on the mean of that subhistogram. It is provided as,

$$V_1 = \frac{1}{I_1 - I_0 + 1} \times \sum_{j=I_0}^{I_1} H(j) \tag{23}$$

$$V_2 = \frac{1}{I_2 - I_1} \times \sum_{j=I_1+1}^{I_2} H(j) \tag{24}$$

$$V_3 = \frac{1}{I_3 - I_2} \times \sum_{j=I_2+1}^{I_3} H(j) \tag{25}$$

$$V_4 = \frac{1}{I_4 - I_3} \times \sum_{j=I_3+1}^{I_4} H(j) \tag{26}$$

V_1, V_2, V_3 *and* V_4 represent the threshold levels calculated for each sub-histogram and $H(j)$ indicates the histogram of an original image. The clipped histogram $H_c(j)$ is produced as follows:

$$H_c(j) = \begin{Bmatrix} H(j) H(j) < V_1 \\ V_1 H(j) \ge V_1 \end{Bmatrix} \ I_0 \le j \le I_1 \tag{27}$$

$$H_c(j) = \begin{Bmatrix} H(j) H(j) < V_2 \\ V_2 H(j) \ge V_2 \end{Bmatrix} \ I_1 \le j \le I_2 \tag{28}$$

$$H_c(j) = \begin{Bmatrix} H(j) H(j) < V_3 \\ V_3 H(j) \ge V_3 \end{Bmatrix} \ I_2 \le j \le I_3 \tag{29}$$

$$H_c(j) = \begin{Bmatrix} H(j) H(j) < V_4 \\ V_4 H(j) \ge V_4 \end{Bmatrix} \ I_3 \le j \le I_4 \tag{30}$$

Since the equalization procedure is carried out separately for each sub-histogram, the intensity variation of each sub-histogram stays within its allowed range. The mapping method preserves average brightness and minute features at all scales, resulting in natural improvement. It is provided as,

$$p_1 = (J-1)\frac{I_1 - I_0 + 1}{I_4 - I_0 + 1} \tag{31}$$

$$p_2 = (J-1)\frac{I_2 - I_1}{I_4 - I_0 + 1} + p_1 \tag{32}$$

International Journal on Recent and Innovation Trends in Computing and Communication
ISSN: 2321-8169 Volume: 11 Issue: 8s
DOI: https://doi.org/10.17762/ijritcc.v11i8s.7205
***Article Received**: 23 April 2023 **Revised:** 10 June 2023 **Accepted:** 28 June 2023*

$$p_3 = (J-1)\frac{I_3 - I_2}{I_4 - I_0 + 1} + p_2 \quad (33)$$

Here, the lowest intensity value is equal to $p_0 = 0$, while the greatest value is equal to $p_4 = J - 1$. Once the sub-histograms have been mapped, their new dynamic ranges are $[p_0 : p_1], [p_{1+1} : p_2], [p_{2+1} : p_3]\ and\ [p_{3+1} : p_4]$. The transformation of each division into a distinct dynamic range. The PDF for every sub-histogram is calculated during this equalization procedure and is provided by:

$$PDF_1(J) = \frac{H_c(j)}{P_1} \quad for\ \ I_0 < j \le I_1 \quad (34)$$

$$PDF_2(J) = \frac{H_c(j)}{P_2} \quad for\ \ I_1 < j \le I_2 \quad (35)$$

$$PDF_3(J) = \frac{H_c(j)}{P_3} \quad for\ \ I_2 < j \le I_3 \quad (36)$$

$$PDF_4(J) = \frac{H_c(j)}{P_4} \quad for\ \ I_3 < j \le I_4 \quad (37)$$

In this case, $P_1, P_2, P_3\ and\ P_4$ stand for the total number of pixels within the clipped histogram. Then the CDF for each sub-histogram is calculated and provided by:

$$CDF_1(j) = \sum_{j=I_0}^{I_1} PDF_1(j) \quad (38)$$

$$CDF_2(j) = \sum_{j=I_1+1}^{I_2} PDF_2(j) \quad (39)$$

$$CDF_3(j) = \sum_{j=I_3+1}^{I_3} PDF_3(j) \quad (40)$$

$$CDF_4(j) = \sum_{j=I_3+1}^{I_4} PDF_4(j) \quad (41)$$

The transfer functions for each sub-histogram are determined via the CDF and is provided by:

$$E_1(j) = p_1 \times CDF_1(j) \quad (42)$$

$$E_2(j) = (p_1 + 1) + (p_2 - (p_1 + 1)) \times CDF_2(j) \quad (43)$$

$$E_3(j) = (p_2 + 1) + (p_3 - (p_2 + 1)) \times CDF_3(j) \quad (44)$$

$$E_4(j) = (p_3 + 1) + (p_4 - (p_3 + 1)) \times CDF_4(j) \quad (45)$$

Utilizing the transfer mentioned above functions, each division is equalized separately. The improved intensity $\{i_m(x,y)\}$ is created by integrating all four sub-images. The aforementioned increased intensity is combined with the saturation and hue space to create an output-enhanced image, which is described by,

$$[r(x,y), g(x,y), b(x,y)] = E_{hsi}^{rgb}[h(x,y), s(x,y), i_m(x,y)] \quad (46)$$

After pre-processing, the colour and texture features are extracted to obtain the required CCT-based information. The Local Intensity Grouping Order Pattern (LIGOP) operator extracts the texture features. The colour features are extracted by determining the terms like mean, standard deviation, skewness, energy, smoothness and variance of the RGB colour space.

B. Feature extraction

Feature extraction is an important stage before classification. An effective feature extraction method can reduce the features and processing time. In here. There are two feature extracting techniques are used, which detailed description is given below:

The texture features are extracted using Local Intensity Grouping Order Pattern (LIGOP) operator. The proposed LIGOP operator investigates local ordinal data to describe the intensity connections between adjacent sample points for each centre pixel. A rotation-invariant grouped order encoding approach is developed, partitioning nearby sample points into groups according to a dominating direction and encoding the GroupWise intensity order connections. For order encoding, identifying the dominating direction is essential. By substituting the average grey value of a local image patch surrounding the sample spot for the grey value of each sampling point, which can accurately predict the prevailing direction. Initially, calculating the average grey values of local image patches surrounding a given centre pixel c in an image R and its neighbouring sample points:

$$\hat{I}_x = \theta(L_{x,k}) \quad (47)$$

$$\hat{I}_{j,b} = \theta(L_{j,b,k}) \quad (48)$$

where $L_{j,b,k}$ stands for a local image patch around the b^{th} neighbouring sampling point and $L_{x,k}$ stands for a local image patch of size $k \times k$ around the central pixel c. $\theta(.)$ is a function that returns the average grey value of an image patch. In addition to enhancing noise resilience, the patch sampling structure used in LIGOP also collects data on larger-scale texture structures. From this point forward, the approach

International Journal on Recent and Innovation Trends in Computing and Communication
ISSN: 2321-8169 Volume: 11 Issue: 8s
DOI: https://doi.org/10.17762/ijritcc.v11i8s.7205
***Article Received**: 23 April 2023 **Revised:** 10 June 2023 **Accepted:** 28 June 2023*

automatically utilizes the average grey values as pixel intensities. The next step is to rotate the adjacent sample points according to their prevailing direction to create a rotation-invariant sampling sequence. The dominating direction is indicated by the index of an adjacent sample point with the greatest grey difference from the centre pixel:

$$Q = \underset{b\in\{0,1,\ldots,B-1\}}{\arg\max} \left| \hat{I}_{j,b} - \hat{I}_x \right| \tag{49}$$

The noise resistance and discriminative ability of computed characteristics can be enhanced using maximum difference responses. Rotate the sample sequence in a circle after determining the dominating direction until the point Q appears in the first location:

$$\left(\hat{I}^*_{j,0},\ldots\hat{I}^*_{j,B-1}\right) := \left(\hat{I}_{j,Q,}\ldots,\hat{I}_{j,B-1},\hat{I}_{j,0},\ldots,\hat{I}_{j,Q-1}\right) \tag{50}$$

Element-wise assignments are made using the symbol"":=in this case. The points in every category are then consistently distributed on the circle after being evenly divided into numerous groups from the points in the rotational sample sequence. The number of points is restricted for every four groups, resulting in $d = B/4$ groups overall for each sampling sequence, i.e., minimal dimensionality of encoded characteristics.

$$\hat{I}^*_y \begin{cases} \left(\hat{I}^*_{j,0},\hat{I}^*_{j,d},\hat{I}^*_{j,2d},\hat{I}^*_{j,3d}\right) & y=1 \\ \left(\hat{I}^*_{j,1},\hat{I}^*_{j,d+1},\hat{I}^*_{j,2d+1},\hat{I}^*_{j,3d+1}\right) & y=2 \\ \vdots & \vdots \\ \left(\hat{I}^*_{j,d-1},\hat{I}^*_{j,2d-1},\hat{I}^*_{j,3d-1},\hat{I}^*_{j,B-1}\right) & y=d \end{cases} \tag{51}$$

Where $\hat{I}^*_y(y=1,\ldots,d)$ is a vector and its components are the grey values of the y^{th} group of nearby sample points. In each category, the connections between the adjacent sample points are encoded in terms of intensity order:

$$Z_{j,B,y} = h\left(\lambda\left(\hat{I}^*_y\right)\right) \tag{52}$$

Where $h(\cdot)$ is a function for mapping that changes each index vector to a distinct integer (this may be accomplished via a lookup table) and $\lambda(\cdot)$ represents an ordered function that arranges vector components in non-descending order as well as returns an index vector representing sorted items. According to Equation (52), the y^{th} group of nearby sample points for pixel C shall be encoded in one of 24 (= 4!) potential values of integers (i.e., LIGOP codes). The proposed LIGOP operator possesses the following characteristics. Initially, grouping creates compact codes, resulting in a low-dimensional histogram representation. An extremely high-dimensional LIGOP histogram (with a minimum of 8! dimensions, provided that the quantity of neighbouring sample points P is commonly specified as 8 and higher) will result from not adopting the grouping. A huge number of LIGOP codes could be created for all conceivable order permutations. Furthermore, by employing a local dominating direction and data on intensity order, the calculated LIGOP codes resist both light and image rotation changes. Additionally, LIGOP encodes local characteristics such as local difference magnitudes, local dominating directions and neighbouring intensity order information, even though these qualities are unavailable in the LBP operator. The colour features are extracted by determining the terms like mean, standard deviation, skewness, energy, smoothness and variance of the RGB colour space.

The average brightness of an image is determined using the mean. The representation is given by Equation (53). Variance is a characteristic that describes how greyscale values might vary, and variance is defined in Equation (54). Standard deviation is used in Equation (55) to define a collection of image contrasts. Equation (56) formulates the characteristic of skewness as an asymmetry of the average intensity. Equation (57) may compute the energy required to measure the distribution of pixel intensities towards the achieved grey level. The intensity of an image's fineness or roughness is measured using the smoothness metric. Equation (58) allows for the calculation of smoothness.

$$mean = \sum_{i=0}^{L-1} ip(i) \tag{53}$$

$$\text{var}\,ience = \sum_{i=1}^{L-1} (i-m)^2\, p(i) \tag{54}$$

$$s\tan dard\ deviation = \sqrt{\sum_{i=1}^{L-1} (i-m)^2\, p(i)} \tag{55}$$

$$skewness = \sum_{i=1}^{L-1} (i-m)^3\, p(i) \tag{56}$$

$$energy = \sum_{i=1}^{L-1} [\, p(i)]^2 \tag{57}$$

$$smoothness = 1 - \frac{1}{1-(s\tan dard\ deviation)^2} \tag{58}$$

Finally, a novel Deep Convolutional Attention-based Bidirectional Recurrent Neural Network (DCA_BRNNet) model is introduced, employing the recovered features to evaluate the CCT values from the provided images.

International Journal on Recent and Innovation Trends in Computing and Communication
ISSN: 2321-8169 Volume: 11 Issue: 8s
DOI: https://doi.org/10.17762/ijritcc.v11i8s.7205
***Article Received**: 23 April 2023 **Revised:** 10 June 2023 **Accepted:** 28 June 2023*

C. CCT estimation using DCA_BRNNet

There are multiple convolutional layers in CNN. The ability of convolutional layers to autonomously arrange input data characteristics during training to increase recognition accuracy has been demonstrated. There are several kernels (or filters) related to the input data. The CNN kernels are data-driven and selected as part of a supervised training procedure to maximize activation, as shown in Equation (59).

$$d_{x,y} = n\left(\sum_{p=1}^{W}\sum_{q=1}^{R} h_{p,q} \cdot i_{x+p,y+q} + f\right) \tag{59}$$

Within the layer of a feature map k, $d_{x,y}$ represents the y^{th} sample. The non-linear function is represented by n where a sigmoid function is used in this research. The convolution kernel weight matrix is referred to as $h_{p,q}$. The dimensions in of $W \times R, f$ on the bias value in the feature map. The upper neuron is linked at an activation value at (x, y) denotes as $i_{x+p,y+q}$. From the available data, DCNN may learn features with increasing levels of complexity.

Like a max-pooling layer, a convolution layer frequently collaborates with a pooling layer to prevent feature errors. To limit the number of parameters required for the computation, the max-pooling layer also helps to reduce the dimensionality of a derived feature map. Additionally, it can provide what is referred to as "spatial variance" to classify the target movements better. Equation (60) provides the output of a max-pooling layer.

$$m_{x,y} = \max_{v \in V}(d_x \times S + v, y) \tag{60}$$

Where, the pooling stride is represented as S and the size of a pooling layer is represented as V.

Recurrent neural networks (RNNs) offer a relatively direct solution for modelling RGB data. The accuracy of RNNs still suffers when the pattern duration is excessively long. Bidirectional Recurrent Neural Networks (BRNNs) are used in the proposed model to address this issue since they can be trained to utilize any input visit data from both directions and have higher accuracy. However, the Recurrent Neural Networks version that addresses the issue of vanishing gradients, including Gated Recurrent Unit (GRU) and Long-Short Term Memory (LSTM) is referred to as "RNNs" in this context. GRU is employed in this research solution to adaptively capture relationships between texture and colour features.

Using both backward and forward RNNs, bidirectional recurrent neural networks are created. When an input sequence is given in the range from z_1 to z_m, the forward RNN $\vec{h}$ computes a series of forward hidden states $\left(\vec{f}_1, \ldots, \vec{f}_m\right)$, where $\vec{f}_p \in R^i$ *and* i denote the dimensionality of hidden states. When the input sequence is read by the backward RNN $\overleftarrow{h}$ in reverse order, from z_m to z_1, a series of backwards hidden states $\left(\overleftarrow{f}_1, \ldots, \overleftarrow{f}_m\right)\left(\overleftarrow{f}_p \in R^i\right)$ are created. The final latent vector representation is determined by $f_p = \left[\vec{f}_p ; \overleftarrow{f}_p\right]^m \left(f_p \in R^{2i}\right)$, which concatenates the forward hidden state $\vec{f}_p$ and the backward one $\overleftarrow{f}_p$. The data from a following sequences is only used to train the model. Only past test results are applied to subsequent visits during testing.

Location-based Attention: The weights are only derived from the current hidden state and are calculated using a location-based attention function in the manner shown below:

$$\beta_{np} = W_\beta^{\mathrm{T}} f_p + a_\beta \tag{61}$$

where $W_\beta \in R^{2i}$ *and* $a_\beta \in R$ are the necessary learning parameters. Using the softmax function, an attention weight vector β_n is derived following Equation (61), as shown below.

$$\beta_n = soft\max\left(\beta_{n1}, \beta_{n2}, \ldots \beta_{n(n-1)}\right) \tag{62}$$

The weights from Equation (62) and the hidden states from f_1 *to* f_{n-1}may then be used to compute the context vector $l_n \in R^{2i}$ in the manner shown below.

$$l_n = \sum_{p=1}^{n-1} \beta_{np} f_i \tag{63}$$

The loss function of a proposed DCA_BRNNet is given by:

$$Loss\ function = \frac{1}{z}\sum_{z=1}^{Z}\left(o_z - \hat{o}_z\right) \tag{64}$$

Where o_z is the actual value and $\hat{o}_z$ is the predicted value with the total iteration of Z. To reduce the loss function, a metaheuristic algorithm is used. The algorithm optimizes the parameter depending on the fitness function:

$$Fitness = MIN\left[Error\right] \tag{65}$$

The Coati Optimisation Algorithm (COA) is used to fine-tune the parameters of a proposed classifier and produces superior performance results.

International Journal on Recent and Innovation Trends in Computing and Communication
ISSN: 2321-8169 Volume: 11 Issue: 8s
DOI: https://doi.org/10.17762/ijritcc.v11i8s.7205
***Article Received**: 23 April 2023 **Revised:** 10 June 2023 **Accepted:** 28 June 2023*

1) Coati Optimization Algorithm

The Coati Optimization Algorithm (COA) [21] is a community-based metaheuristic, and coatis are regarded as members of the population. Each coati's exact placement within the search area determines the values for the decision variables. As a result, coatis' place in the COA proposed a potential answer to the dilemma. When the COA execution initiates, Equation (66) randomly initializes coatis' positions in the search space.

$$P_x : P_{x,y} = lb_y + R \cdot \left(ub_y - lb_y\right), x = 1,2,\ldots A,\ y = 1,2,\ldots B \tag{66}$$

where P_x is the x^{th} search agent position in search space, $P_{x,y}$ is the y^{th} decision variable's value, A is the total search agents, B represents the number of decision variables, R represents a random real number within the interval [0, 1] and ub_y *and* lb_y are the upper and lower bounds of the y^{th} decision variable, respectively. The search agent's population in a COA is mathematically expressed by the following matrix P, known as the population matrix.

$$P = \begin{bmatrix} P_1 \\ \vdots \\ P_x \\ \vdots \\ P_A \end{bmatrix}_{A\times B} = \begin{bmatrix} P_{1,1} & \cdots & P_{1,y} & \cdots & P_{1,B} \\ \vdots & & \vdots & & \vdots \\ P_{x,1} & \cdots & P_{x,y} & \cdots & P_{y,B} \\ \vdots & & \vdots & & \vdots \\ P_{A,1} & \cdots & P_{A,y} & \cdots & P_{A,B} \end{bmatrix}_{A\times B} \tag{67}$$

The estimation of possible values for the problem's fitness function occurs due to the insertion of candidate solutions into decision variables. Equation (68) is used to display these values.

$$V = \begin{bmatrix} V_1 \\ \vdots \\ V_x \\ \vdots \\ V_A \end{bmatrix}_{A\times 1} = \begin{bmatrix} V(P_1) \\ \vdots \\ V(P_x) \\ \vdots \\ V(P_A) \end{bmatrix}_{N\times 1} \tag{68}$$

Where V_x is the value of the generated fitness function determined by the x^{th} search agent and V is the vector of the obtained fitness function. The resultant value of a fitness function is used in metaheuristic algorithms to determine the quality of a candidate solution. Because of this, the best population member is the one who determines the best value for the fitness function. The algorithm rounds alter the possible solutions, thus each iteration also updates the population's best performance.

Attacking and Hunting approach for food (exploration phase)

The initial part of upgrading search agent's populations in the search has been completed. Space is modelled by replicating their attack tactics on foods. A gang of search agents climbing the branches to intimidate a food. Some more search agents wait for the food to fall to the ground under a tree. The search agents pursue and hunt the food once it has fallen to the ground. This method causes search agents to travel across the search space, demonstrating the COA's capacity to explore in global search.

Within the COA design, the food is given the position of the most successful community member. Additionally, it is thought that half of the hunters climb the tree while the other half wait for the food to hit the ground. Equation (69) is therefore used to mathematically reproduce the position of a search agent ascending from the tree.

$$P_x^{I1} : P_{x,y}^{I1} = p_{x,y} + R \cdot \left(IG_y - X \cdot p_{x,y}\right), \text{ for } x = 1,2,\left\lfloor \frac{A}{2} \right\rfloor \text{ and } y = 1,2,\cdots B \tag{69}$$

When the food drops to the earth's surface, it will be randomly placed in search space. Search agents on the surface travel in the search space according to this random location, as modelled by Equations (70) and (71).

$$IG^G : IG_y^G = lb_y + R \cdot \left(ub_y - lb_y\right),\ y = 1,2,\cdots B \tag{70}$$

$$p_x^{I1} : p_{x,y}^{I1} = \begin{cases} p_{x,y} + R \cdot \left(IG_y^G - X \cdot p_{x,y}\right), & V_{IG^G} < V_x \\ p_{x,y} + R \cdot \left(p_{x,y} - IG_y^G\right), & else \end{cases} \tag{71}$$

Each search agent's new location estimation is appropriate for the update operation if it increases the accuracy of a fitness function; otherwise, the search agent stays in the previous location. This updating condition is replicated with Equation (72) for $x = 1,2,\cdots A$.

$$P_x = \begin{cases} P_x^{I1}, & V_x^{I1} < V_x \\ P_x, & else \end{cases} \tag{72}$$

Here, P_x^{I1} is the latest location determined for the x^{th} search agent, $P_{x,y}^{I1}$ is its y^{th} dimension, V_x^{I1} is its fitness function value, R is a random real number in the interval [0, 1], IG reflects the food's location inside the area of search, which indicates the current location of the best member, IG_y is its y^{th} dimension, X is an integer which is chosen at random from the set [1,2], IG^G is the food's location on the surface of a ground, which is created at random, IG_y^G is its y^{th} dimension, V_{IG^G} is its fitness function value and $\lfloor \cdot \rfloor$ is its floor function (which is also referred to as the best integer function).

The process of escaping from predators (exploitation phase)

International Journal on Recent and Innovation Trends in Computing and Communication
ISSN: 2321-8169 Volume: 11 Issue: 8s
DOI: https://doi.org/10.17762/ijritcc.v11i8s.7205
***Article Received**: 23 April 2023 **Revised:** 10 June 2023 **Accepted:** 28 June 2023*

The next part of a procedure of updating search agents' positions in the search space is mathematically modelled based on search agents' natural behavior while confronting predators and escaping from predators. When a predator assaults a search agent, the search agent flees. The COA's ability to use local search is demonstrated by search agent's moves in this approach, which placed it in an optimal position comparable to where it is at present. To imitate this behaviour, a random position around the location of each search agent is created using Equations (73) and (74).

$$lb_y^{local} = \frac{lb_y}{f}, ub_y^{local} = \frac{ub_y}{f}, where\ f = 1,2,\cdots F \tag{73}$$

$$P_x^{I2} : p_{x,y}^{I2} = p_{x,y} + (1-2R)\cdot\left(lb_y^{local} + R\cdot\left(ub_y^{local} - lb_y^{local}\right)\right), x = 1,2,\ldots A, y = 1,2,\cdots B \tag{74}$$

The newly estimated position is suitable if it enhances the value of a goal function that this condition replicates using Equation (75).

$$P_x = \begin{cases} P_x^{I2}, & V_x^{I2} < V_x \\ P_x, & else \end{cases} \tag{75}$$

Here, P_x^{I2} is the latest location determined for the x^{th} search agent using the following stage of COA, $P_{x,y}^{I2}$ is its y^{th} dimension, and V_x^{I2} is its fitness function's value, r is a random number within the period [0, 1], t is an iteration counter, lb_y^{local} and ub_y^{local} are the local lower bound and local upper bound of the y^{th} decision variable, respectively. Figure 2 represents the flowchart of an optimization algorithm.

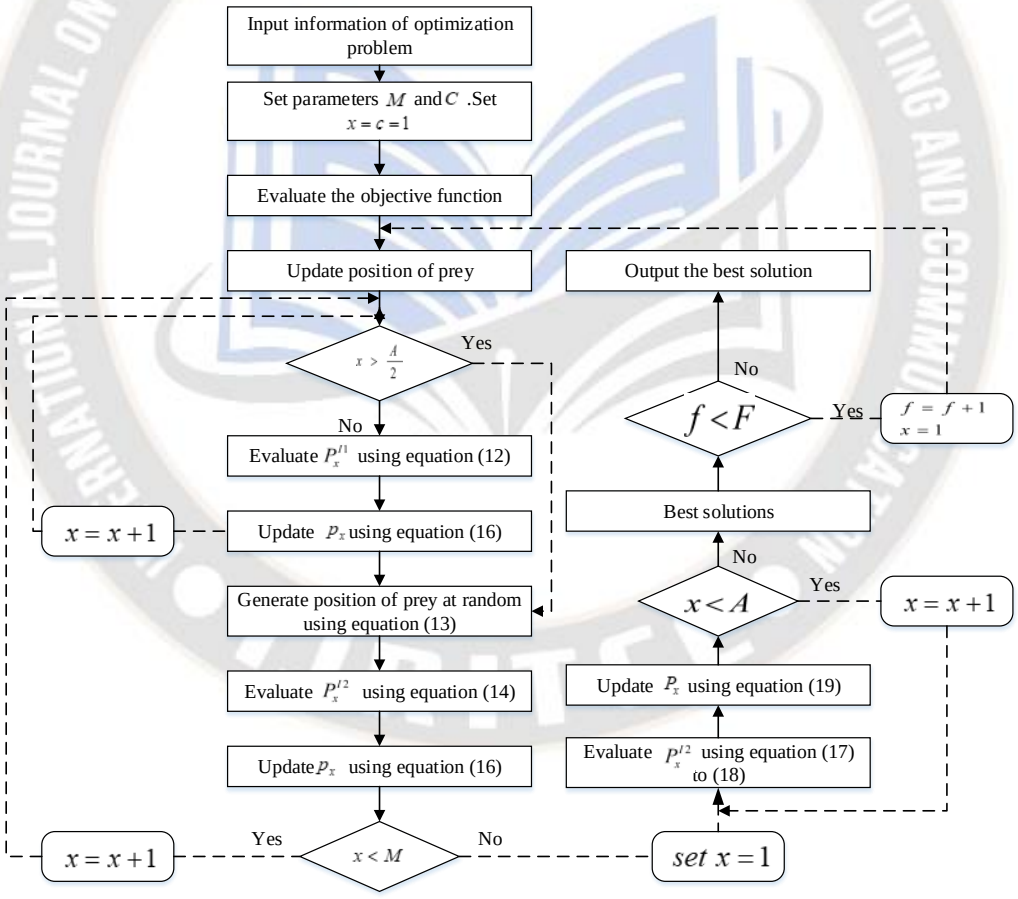

Figure 2: Flowchart of COA algorithm

IV. RESULT AND DISCUSSION

The proposed model is implemented in the Python platform. An Intel(R) Core(TM) i5-3470 CPU operating at 3.20 GHz,

International Journal on Recent and Innovation Trends in Computing and Communication
ISSN: 2321-8169 Volume: 11 Issue: 8s
DOI: https://doi.org/10.17762/ijritcc.v11i8s.7205
***Article Received**: 23 April 2023 **Revised:** 10 June 2023 **Accepted:** 28 June 2023*

8GB of installed RAM, a 64-bit operating system, and an x64-based processor are used to implement this work. This section compares McCamys's, Hernandez's and Catalbas's methods with the proposed model by varying CCT values. A collection of 191 RGB images and their matching CCT values was developed. The RGB images in the database were generated using the CIE 1931 colour space. Table 1 represents the CCT value of various light sources.

Table 1: CCT values of various Light source

Temperature	Light source
1700 K	Match flame
1850 K	Candle flame, sunset/sunrise
2400 K	Standard incandescent lamps
2550 K	Soft white incandescent lamps
2700 K	Soft white compact fluorescent
3000 K	Warm white compact fluorescent
3200 K	Studio lamps
5000 K	Horizon daylight
6500 K	Daylight, overcast
6500 – 9500 K	LCD or CRT screen
15000 – 27000 K	Clear blue pole ward sky

Figure 3 represents the proposed model's actual CCT value and estimated CCT value. This efficiency can be observed in the CCT values obtained after using the RGB images to create the network structure database. Prediction and real CCT values fluctuate similarly, and the network topology has no overfitting.

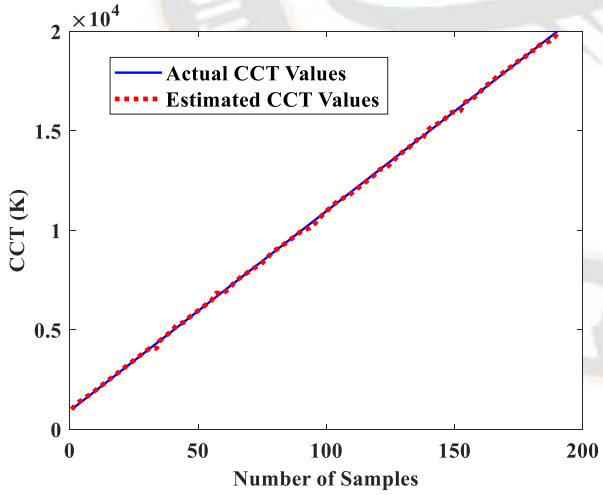

Figure 3: Original and Ideal CCT values

Table 2 contains statistical characteristics related to the discrepancy between real and estimated CCT values. The dataset model was estimated with a mean error of less than 50 K using CCT values ranging from 1000 K to 20,000 K. In addition, if the extra statistical variables acquired in Table 2 are analyzed, the proposed framework exhibits resilient properties in the CCT estimation method. Obviously, the proposed CNN-based deep regression approach effectively learns the association between RGB images in the produced database and their respective CCT values.

Table 2: Estimation difference

Values	Parameter
2K	Minimum
41K	Mean
56K	RMSE
276K	Maximum
38K	Standard deviation

As the number of iterations rises, Figure 4 illustrates how the value of an RMSE for the produced network architecture varies. It can be shown that the recommended CNN network setup successfully learned this dataset, which was created to predict CCT values based on RGB images.

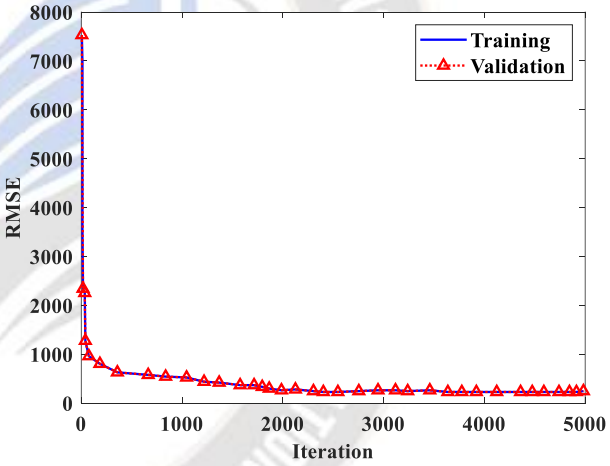

Figure 4: Training and testing using varying RMSE

Table 3 compares various methods in terms of MSE and RMSE. McCamys's, Hernandez's and Catalbas's methods are compared with the proposed model.

Table 3: MSE and RMSE values of various methods

Algorithm	MSE	RMSE
McCamys's,	1905K	2002K
Hernandez's	1887K	2004K
Catalbas's	566K	633K
Proposed	529K	587K

Figure 5 depicts the histogram distribution of CCT images acquired using various techniques. The proposed technique properly predicts the CCT distribution on the image, as evidenced by the histogram plots of CCT values. The CCT distribution's greatest value based on the proposed technique is

International Journal on Recent and Innovation Trends in Computing and Communication
ISSN: 2321-8169 Volume: 11 Issue: 8s
DOI: https://doi.org/10.17762/ijritcc.v11i8s.7205
***Article Received**: 23 April 2023 **Revised:** 10 June 2023 **Accepted:** 28 June 2023*

around 7000 K. The highest limit of maximum histogram values is around 10000 K, and these CCT values are significantly higher than the real value of 6500 K. In this case, the proposed method provides an effective outcome for directly determining CCT values from RGB images. Table 4 represents the values of a proposed model in each CCT value.

Table 4: Frequency vs CCT

CCT values (K)	Frequency
265	494.785
795	732.154
1325	2157.245
1855	4887.158
2385	5648.752
2915	7367.545
3445	9485.348
3975	8200.695
4505	9852.212
5035	6501.248
5565	3298.667
6095	1784.348
6625	808.284
7155	354.158

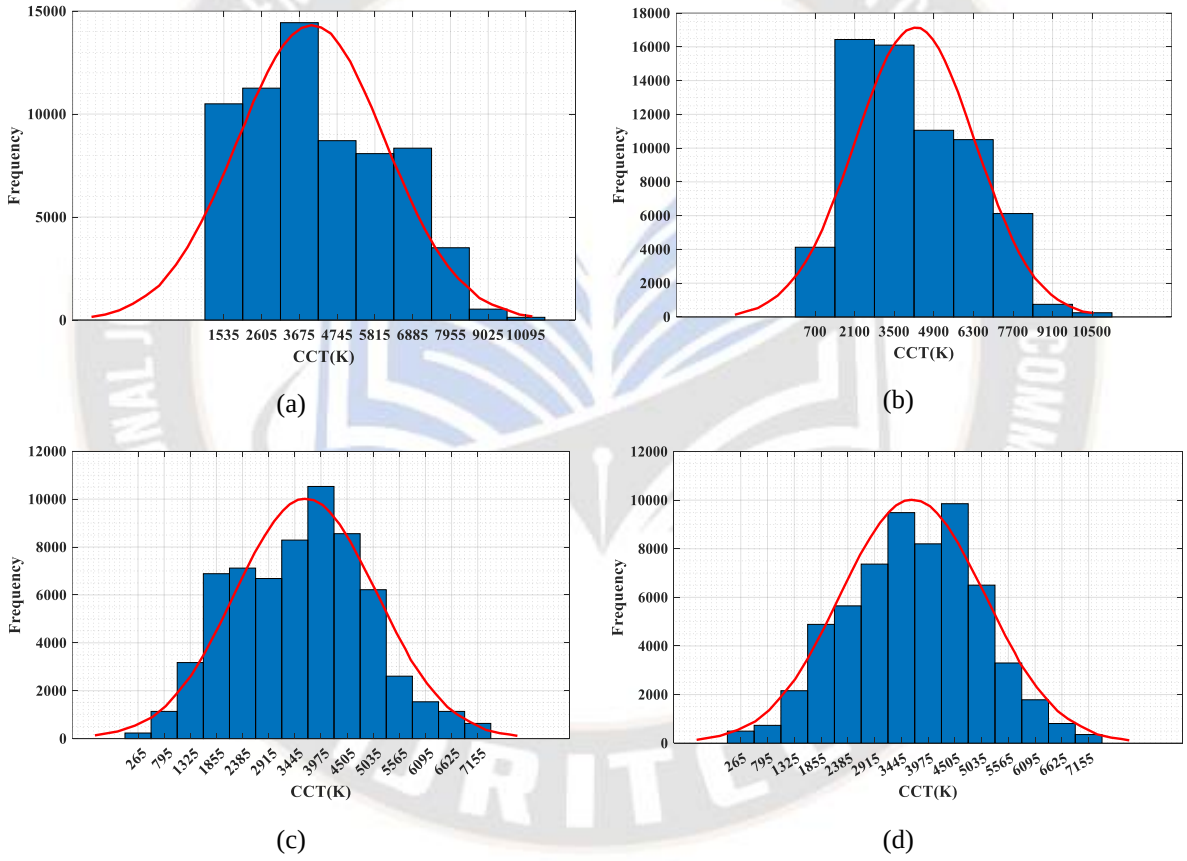

Figure 5: (a) McCamys's method, (b) Hernandez's method, (c) Catalbas's method, (d) the proposed method

V. CONCLUSION AND FUTURE SCOPE

The proposed study includes image collection, pre-processing, feature extraction and CCT assessment. The input RGB images are initially created using the CIE 1931 colour space. The raw input samples are then pre-processed to improve image quality by conducting image cropping and scaling, denoising by hybrid median-wiener filtering, and contrast enhancement via Rectified Gamma based Quadrant Dynamic Clipped Histogram Equalisation (RG_QuaDy_CHE). After pre-processing, the colour and texture characteristics are removed to obtain the necessary CCT-based information. The Local Intensity Grouping Order Pattern (LIGOP) operator retrieves the texture characteristics. At the same time, the colour features are extracted using the RGB colour space's mean, standard deviation, skewness, energy, smoothness and variance. Finally, the CCT values were calculated from the provided photos

International Journal on Recent and Innovation Trends in Computing and Communication
ISSN: 2321-8169 Volume: 11 Issue: 8s
DOI: https://doi.org/10.17762/ijritcc.v11i8s.7205
***Article Received**: 23 April 2023 **Revised:** 10 June 2023 **Accepted:** 28 June 2023*

utilizing the retrieved features by adding a novel Deep Convolutional Attention-based Bidirectional Recurrent Neural Network (DCA_BRNNet) model. The Coati Optimisation Algorithm (COA) is used to modify the suggested classifier's parameters and achieve better performance outcomes. The proposed model is compared with several current approaches in the results section and achieves an MAE value of 529K and an RMSE value of 587K, respectively. In the future, this research would like to explore other properties of more datasets and compare existing methods. Researchers like to use secondary colours as input while also evaluating their performance.

REFERENCE

[1] Y. Yi, J. Wang, W. Zhou, C. Zheng, J. Kong, and S. Qiao, "Non-negative matrix factorization with locality constrained adaptive graph," *IEEE Transactions on circuits and systems for video technology*, vol. 30, no. 2, pp. 427-441, 2019.

[2] N. Yu, Y. Lv, X. Liu, S. Jiang, H. Xie, X. Zhang, and K. Xu, "Impact of Correlated Color Temperature on Visitors' Perception and Preference in Virtual Reality Museum Exhibitions," *International Journal of Environmental Research and Public Health*, vol. 20, no. 4, pp. 2811, 2023.

[3] M. Awada, B. Becerik-Gerber, S. Hoque, Z. O'Neill, G. Pedrielli, J. Wen, and T. Wu, "Ten questions concerning occupant health in buildings during normal operations and extreme events including the COVID-19 pandemic," *Building and Environment*, vol. 188, pp. 107480, 2021.

[4] K.M. Zielinska-Dabkowska, J. Hartmann, and C. Sigillo, "LED light sources and their complex set-up for visually and biologically effective illumination for ornamental indoor plants," *Sustainability*, vol. 11, no. 9, pp. 2642, 2019.

[5] A. Wawrzyniak, "A Light Booster metro car for the commuting work force: Human Centric Lighting in underground transportation," 2019.

[6] W. Luo, R. Kramer, M. Kompier, K. Smolders, Y. de Kort, and W.V. Marken Lichtenbelt, "Effects of correlated color temperature of light on thermal comfort, thermophysiology and cognitive performance," *Building and Environment*, vol. 231, pp. 109944, 2023.

[7] S. Hu, M. He, G. Liu, M. Lu, P. Liang, and F. Liu, "Correlation between the visual evoked potential and subjective perception at different illumination levels based on entropy analysis," *Building and Environment*, vol. 194, pp. 107715, 2021.

[8] K. Yin, E. Hsiang, J. Zou, Y. Li, Z. Yang, Q.Yang, P. Lai, C. Lin, and S. Wu, "Advanced liquid crystal devices for augmented reality and virtual reality displays: principles and applications," *Light: Science & Applications*, vol. 11, no. 1, pp. 161, 2022.

[9] E.J. Ricketts, D.S. Joyce, A.J. Rissman, H. J. Burgess, C.S. Colwell, L.C. Lack, and M. Gradisar, "Electric lighting, adolescent sleep and circadian outcomes, and recommendations for improving light health," *Sleep Medicine Reviews*, pp. 101667, 2022.

[10] S.T. Peeters, K.C. Smolders, and Y.A. de Kort, "What you set is (not) what you get: How a light intervention in the field translates to personal light exposure," *Building and Environment*, vol. 185, pp. 107288, 2020.

[11] O. Kardan, A.J. Stier, C. Cardenas-Iniguez, J.C. Pruin, K.E. Schertz, Y. Deng, T. Chamberlain et al, "Adult neuromarkers of sustained attention and working memory predict inter-and intra-individual differences in these processes in youth," *BioRxiv*, pp. 2021-08, 2021.

[12] Ana Rodriguez, Kristinsdóttir María, Pekka Koskinen Pieter van der Meer, Thomas Müller. Machine Learning Techniques for Multi-criteria Decision Making in Decision Science. Kuwait Journal of Machine Learning, 2(4). Retrieved from http://kuwaitjournals.com/index.php/kjml/article/view/214

[13] K.E. Smith, T. B. Mason, L.M. Schaefer, A. Juarascio, R. Dvorak, N. Weinbach, R. D. Crosby, and S.A. Wonderlich, "Examining intra-individual variability in food-related inhibitory control and negative affect as predictors of binge eating using ecological momentary assessment," *Journal of psychiatric research*, vol. 120, pp. 137-143, 2020.

[14] S. Jiang, L. Postovit, A. Cattaneo, E.B. Binder, and K. J. Aitchison, "Epigenetic modifications in stress response genes associated with childhood trauma," *Frontiers in psychiatry*, vol. 10, pp. 808, 2019.

[15] Ansari , A. S. . (2023). Numerical Simulation and Development of Brain Tumor Segmentation and Classification of Brain Tumor Using Improved Support Vector Machine. International Journal of Intelligent Systems and Applications in Engineering, 11(2s), 35–44. Retrieved from https://ijisae.org/index.php/IJISAE/article/view/2505

[16] S.R. Coleman, A.L. Pincus, and J.M. Smyth, "Narcissism and stress-reactivity: A biobehavioural health perspective," *Health Psychology Review*, vol. 13, no. 1, pp. 35-72, 2019.

[17] M.A. Martínez-Domingo, M. Melgosa, K. Okajima, V.J. Medina, and F.J. Collado-Montero, "Spectral image processing for museum lighting using CIE LED illuminants," *Sensors*, vol. 19, no. 24, pp. 5400, 2019.

[18] V. Kamath, C.P. Kurian, and U.S. Padiyar, "Development of Bayesian Neural Network Model to Predict the Correlated Color Temperature Using Digital Camera and Macbeth ColorChecker Chart," *IEEE Access*, vol. 10, pp. 55499-55507, 2022.

[19] S. Oh, G. Jeon, and J. Lim, "Method of Calculating Short-Wavelength-Ratio-Based Color Temperature Supporting the Measurement of Real-Time Natural Light Characteristics through RGB Sensor," *Sensors*, vol. 20, no. 22, pp. 6603, 2020.

[20] S. Oh, and Y. Kwak, "A hue and warm-cool model for warm-cool based correlated color temperature calculation," *Color Research & Application*, vol. 47, no. 4, pp. 953-965, 2022.

[21] M. Magnusson, J. Sigurdsson, S.E. Armansson, M.O. Ulfarsson, H. Deborah, and J.R. Sveinsson, "Creating RGB images from hyperspectral images using a color matching function," *In IGARSS 2020-2020 IEEE International Geoscience and Remote Sensing Symposium*, pp. 2045-2048, 2020. IEEE.

[22] M.E. Kompier, K.C. Smolders, and Y.A. De Kort, "Abrupt light transitions in illuminance and correlated colour temperature result in different temporal dynamics and

International Journal on Recent and Innovation Trends in Computing and Communication
ISSN: 2321-8169 Volume: 11 Issue: 8s
DOI: https://doi.org/10.17762/ijritcc.v11i8s.7205
***Article Received**: 23 April 2023 **Revised:** 10 June 2023 **Accepted:** 28 June 2023*

interindividual variability for sensation, comfort and alertness," *PloS one*, vol. 16, no. 3, p.e0243259, 2021.

[23] M. Dehghani, Z. Montazeri, E. Trojovská, and P. Trojovský, "Coati Optimization Algorithm: A new bio-inspired metaheuristic algorithm for solving optimization problems," *Knowledge-Based Systems*, vol. 259, pp. 110011, 2023.